Decarbonization of heat pump dual fuel systems using a practical model predictive control:
Field demonstration in a small commercial building

Sang woo Ham[1], Lazlo Pau[1]l, Donghun Kim[1], Marco Pritoni[1], Richard Brown[1], Jingjuan (Dove) Feng[2]

[1]Building Technologies & Urban Systems Division, Lawrence Berkeley National Laboratory, [2]Advanced Energy, TRC Companies, Inc.

Disclaimer:

Highlights

Decarbonization of Heat Pump Dual Fuel Systems using a Practical Model Predictive Control: Field Demonstration in a Small Commercial Building[1]

Sang woo Ham, Lazlo Paul, Donghun Kim, Marco Pritoni, Richard Brown, Jingjuan(Dove) Feng

- Implementation of a practical MPC for a heat pump-based dual fuel system in a small commercial building.

- Experimental demonstration of a practical MPC with low-cost sensor retrofits for 2 winter months

- Achievement of 27% energy cost saving and 23% load shifting from occupied-peak time to non-occupied-non-peak time.

- Elimination of natural gas usage with GHG emissions reduction of ∼52kgCO2/month

---

[1]This manuscript is an extension of work originally presented in 2023 ASHRAE Annual Conference at Tampa [1]

Decarbonization of Heat Pump Dual Fuel Systems using a Practical Model Predictive Control: Field Demonstration in a Small Commercial Building[1]

Sang woo Ham[a], Lazlo Paul[a], Donghun Kim[a], Marco Pritoni[a], Richard Brown[a], Jingjuan(Dove) Feng[b]

[a]*Building Technology & Urban Systems Division, Lawrence Berkeley National Laboratory, Berkeley, CA, USA*
[b]*Advanced Energy, TRC Companies, Inc., Windsor, CT, USA*

Abstract

In the transition from fossil fuel to electrified heating, a concerning trend is emerging in certain regions of the US. Owners of buildings with gas-based systems leave them in place after adding heat pumps (HPs). Existing control solutions for these hybrid (dual fuel) systems are rudimentary and fall short of realizing the full carbon reduction potential of these systems. Model predictive control (MPC) is often regarded as the benchmark for achieving optimal control in integrated systems. However, in the case of small-medium commercial buildings (SMCBs), the control and communication infrastructure required to facilitate the implementation of such advanced controls is often lacking. This paper presents a field implementation of easy-to-deploy MPC for a dual fuel heating system consisting of HPs and a gas-fired furnace (GF) for SMCBs. The control system is deployed on an open-source middleware platform and utilizes low-cost sensor devices to be used for real SMCBs without major retrofits. We demonstrated this MPC in a real office building with 5 HPs and 1 GF for 2 months. The test results showed that MPC reduced 27% of cost while completely eliminating GF usage by shifting 23% of the thermal load from occupied-peak time to non-occupied-non-peak times.

Keywords: electrification, decarbonization, dual fuel system, heat pump, MPC, HVAC control

---

Nomenclature

API: Application programming interface

GHG: Greenhouse gas

GF: Gas furnace

HP: Heat pump

HVAC: Heating, ventilation, and air-conditioning

MPC: Model predictive control

M&V: Measurement and verification

RTF: Runtime fraction

---

[1]This manuscript is an extension of work originally presented in 2023 ASHRAE Annual Conference at Tampa [1]

RTU: Rooftop unit

RMSE: Root mean squared error

LD: Lumped disturbance term for all the unmeasured disturbances

$\bar{(\cdot)}$: moving averaged value over a certain time window (e.g., 15-minute for MPC)

$(\mathbf{A}(\cdot), \mathbf{B_u}(\cdot), \mathbf{B_w}(\cdot), \mathbf{C}(\cdot))$**:** A state space model structure that maps θ to building dynamics (i.e., G_u and G_w)

$(\mathbf{A_d}(\cdot), \mathbf{B_{d},}_u(\cdot), \mathbf{B_{d},}_w(\cdot), \mathbf{C_d}(\cdot))$**:** A discretized state space model of $(\mathbf{A}(\cdot), \mathbf{B_u}(\cdot), \mathbf{B_w}(\cdot), \mathbf{C}(\cdot))$

$A_{\mathbf{win},i}$**:** Effective window area of ith zone windows [m^2]

$C_{\mathbf{w},i}$**:** Thermal capacitance of wall mass of ith zone [kWh/K]

$C_{\mathbf{za},i}$**:** Thermal capacitance of zone air of ith zone [kWh/K]

$(\cdot)|k$**:** Set of measured data from time step from timestep from 1 to k.

ER_{el}**:** Electricity cost rate [\$/kWh(el)]

ER_{ng}**:** Natural gas cost rate [\$/kWh(th)]

e_i**:** Zero mean white noise of ith zone

$(\mathcal{F}(\cdot), \mathcal{G}(\cdot))$**:** A state space model structure that maps ρ to lumped disturbance dynamics (i.e., H)

f_i**:** Convective fraction of the incident solar radiation of ith zone windows [-]

$G_{\mathbf{u}}$**:** A dynamic system that maps $\mathbf{u}$ to $\mathbf{y}$

$G_{\mathbf{w}}$**:** A dynamic system that maps $\mathbf{w}$ to $\mathbf{y}$

$G_{\mathbf{g}}$**:** A dynamic system that maps $\dot{Q}_{g,1:n}$ to $\mathbf{y}$

H**:** Dynamics of lumped output disturbances

j**:** Prediction time step

$K_{\mathbf{p}}$**:** Proportional gain [-]

m**:** Number of measured inputs

$P_{\mathbf{HP},i}$**:** Nominal rated power of ith HP [kW]

$P_{\mathbf{GF}}$**:** Nominal rated gas heating rate of GF [kW]

$N_{\mathbf{p}}$**:** Prediction horizon

N**:** Number of data

n**:** Number of heating devices (HPs and GFs)

$\dot{Q}_{\mathbf{g},i}$**:** Unmeasured heat gains of ith zone [kW]

$\dot{q}_{\mathbf{sol,win},i}$: Incident solar radiation per area of ith zone windows [kW/m^2]

$\dot{Q}_{\mathbf{HP},i}$: Estimated heating capacity of ith HP at full speed [kW]

$\dot{Q}_{\mathbf{GF}}$: Estimated heating capacity of GF [kW]

$(R_{\mathbf{zw},i}, R_{\mathbf{zo},i})$: Thermal resistances between temperature nodes of ith zone [K/kW]

$(T_{\mathbf{l}}, T_{\mathbf{u}})$: Lower and upper temperature bounds [°C]

$T_{\mathbf{za},i}$: Air temperature of ith zone [°C]

$T_{\mathbf{hsp},i}$: Heating setpoint of the ith HP [°C]

$T_{\mathbf{hsp,GF}}$: Heating setpoint of the GF [°C]

$T_{\mathbf{w},i}$: Wall thermal mass temperature of ith zone [°C]

$T_{\mathbf{oa}}$: Outdoor air temperature [°C]

t, k: Continuous time and discrete time

$\mathbf{u}$: Vector of control inputs (i.e., RTF of HPs and GF, $[u_{\mathrm{HP},1:n-1}, u_{\mathrm{GF}}]$)

$u_{\mathbf{HP},i}$: Heating signal of ith HP device

$u_{\mathbf{GF}}$: Heating signal of GF device

$\hat{\mathbf{u}}(k)$: Vector of estimated runtime fractions of devices (HPs and GFs) for a sampling time k

$\bar{\mathbf{u}}(k)$: Vector of runtime fractions of device (HPs and GFs) for a sampling time k)

$\mathbf{w}$: Vector of measured disturbances (i.e., $[T_{\mathrm{oa}}, \dot{Q}_{\mathrm{sol,win},1:n}]$)

$\mathbf{x}$: Vector of state variables (i.e., $[T_{\mathrm{w},1:n}, T_{\mathrm{za},1:n}]$)

$\hat{\mathbf{x}}(k|j)$: Vector of estimated(predicted) state variables at time k from the data at j

$\mathbf{y}$: Vector of measured thermostat temperatures for all zones [°C]

$(\Gamma_{\mathbf{l}}, \Gamma_{\mathbf{u}})$: Temperature violations from lower and upper temperature bounds

δ: An upper bound of instantaneous power

ε_i: One step ahead prediction error of ith zone

$\boldsymbol{\zeta}$: Vector of internal state of lumped output disturbances

θ: Physical parameters consisting of thermal resistances and capacitances, $[C_{\mathrm{w},1:n}, C_{\mathrm{za},1:n}, R_{\mathrm{zw},1:n}, R_{\mathrm{zo},1:n},$ $f_{1:n}, A_{\mathrm{win},1:n}, \dot{Q}_{\mathrm{HP},1:n}, \dot{Q}_{\mathrm{GF}}]$

$\boldsymbol{\nu}$: Vector of lumped output disturbances [°C]

ρ: Parameters that construct dynamics of lumped output disturbances, i.e. H

$(\omega_{\mathbf{l}}, \omega_{\mathbf{u}})$: Weights on optimization variables for $(\Gamma_{\mathrm{l}}, \Gamma_{\mathrm{u}})$

$\omega_{\mathbf{d}}$: Weight on optimization variables for δ

1. Introduction

To address the climate crisis, our national leadership is actively developing an accelerated roadmap for decarbonization. Within the building sector, it has become evident that the most effective approach to achieving this goal involves widespread electrification of space and water heating, as well as replacement of natural gas systems [2] typically using heat pump (HP) systems. Many customers choose to install HP systems equipped with an auxiliary heater that operates on electricity or natural gas [3], especially in cold climates [4]. However, it has also been observed that many customers updating their heating systems with HPs retain their existing gas-based systems [5], particularly when installing ductless mini-split heat pumps. The resulting dual fuel systems have diverse and complex configurations, and they may remain in place for more than a decade due to the long lifespan of packaged gas-based systems.

For example, the integration of gas-fired furnaces (GF) and HPs in dual fuel heating systems has been identified as a critical challenge by the New York State Energy Research and Development Authority (NY-SERDA) [6]. In response to this concern, NYSERDA has introduced specifications for integrated controllers that leverage existing control products accessible in the market [6]. Although these controllers present an advancement over separately managing the two systems, they fall short of fully optimizing the hybrid system's performance, curbing greenhouse gas emissions, or minimizing utility expenses.

The absence of advanced controls for dual-fuel systems presents a substantial challenge, particularly in small and medium commercial buildings (SMCBs). These buildings often have systems that are less compatible with conventional control methods (e.g., programmable thermostat), such as infrared (IR) remote control-based ductless mini-split HPs that cannot be easily connected using standardized protocols [7]. Furthermore, a building automation system is typically not available in small buildings, and there are limited control options available specifically tailored for such buildings. This scarcity of control alternatives, coupled with the associated costs and time required to upgrade controls, significantly restricts the accessibility of reliable control solutions for SMCBs. The complexity and diversity of hybrid systems in these buildings, coupled with their unique operational requirements, further complicate the development of an effective control solution.

However, there has been a recent growing trend in SMCBs towards embracing the Internet of Things (IoT) such as WiFi-enabled thermostats [8, 7]. This shift has opened up new possibilities for advanced controls for SMCBs by providing data collection and device control ability in a cost-effective and scalable manner. These systems can be installed with minimal disruption and possess a modular nature, facilitating effortless expansion and customization as the building's requirements evolve.

Model predictive control (MPC) is widely utilized as an advanced control technique for the dynamic operation of heating, ventilation, and air conditioning (HVAC) systems in both research [9] and field implementations [10]. MPC provides optimal HVAC system operation to minimize an objective such as energy cost or greenhouse gas emission (GHG) given the required constraints such as comfort boundaries by using mathematical models for buildings and disturbance forecasts (e.g., weather). Furthermore, MPC has the flexibility to handle various price signals from the grid (e.g., Time-of-Use (TOU) rate, real-time price) to provide grid services [11] such as load shifting.

Typically, MPC has been applied to large commercial buildings with central HVAC systems where a supervisory building automation system (BAS) system is available [12, 13, 14]. However, recent studies have demonstrated that MPC can be applicable for SMCBs with electric rooftop units (RTUs) in a scalable manner. Kim et al. [15] presented a plug-and-play MPC for multiple RTUs for a gymnasium building with 4 RTUs. The MPC showed 8% energy reductions and 40% peak demand reductions by reducing ON/OFF cyclings and overcooling through the coordination of multiple RTUs. Kim and Braun [16] demonstrated an MPC algorithm for multiple ON/OFF RTUs in a small retail store to reduce both energy and peak

4

demand. The MPC reduced about 12% of energy and 18% of peak demand by coordinating RTU operations for several months of trials. Kim and Braun [17] applied a hierarchical MPC algorithm for ON/OFF staged packaged units in a laboratory building. The MPC algorithm is designed to achieve both load shifting and peak demand reduction, resulting in 30% of demand cost savings and 40% of on-peak demand cost savings with less than 10% of cost savings.

MPC for dual fuel systems should integrate two different fuel sources into a single objective function by using energy cost [13]. However, recent studies have focused on reducing natural gas use to reduce carbon emissions. Cotrufo et al. [18] developed a black-box model-based predictive control scenario to reduce greenhouse gas (GHG) emissions by restricting natural gas usage at morning heating peak time through pre-heating by using electric baseboard heaters during non-occupied time, resulting in a 22% reduction in GHG emissions in the real building. However, the predictive control scenario is specifically designed for that particular building by training several predictive control scenarios using data obtained from it. Demirezen and Fung [19] proposed the Smart Dual Fuel Switching System (SDFSS) for a residential dual fuel system. The SDFSS is provided as a cloud-based system and determines the operation of the heat pump and the natural gas boiler based on time-of-use (TOU) pricing, fuel cost, short-term weather forecast, and equipment efficiencies and capacities. Based on the calibrated simulation model, the SDFSS algorithm was tested on various carbon tax levels. Yoon et al. [20] proposed a rule-based control approach for a dual fuel heat pump system to save heating energy and energy costs for cold climates and evaluated its performance in a simulation study. Using the time-of-use electricity rate, the dual fuel heat pump system was able to reduce heating energy by 30.44% over a gas furnace-only system, which also shows 3.66% more savings than the heat pump-only system. Li et al. [21] presented an MPC for a dual fuel system to optimize the GHG and energy costs. The seamlessly fuel flexible heat pump (SFFHP) uses natural gas or heat pump based on the GHG signal and the energy cost for heating operation. Various scenarios of different weights on GHG signal and energy cost were evaluated in the simulation.

In summary, although several simulation studies have demonstrated the potential of MPC to optimize dual fuel systems, the practical applicability and actual cost savings of MPC in real buildings have not yet been assessed. A successful demonstration of MPC in SMCBs with practical constraints (i.e., without necessitating major hardware retrofitting) could accelerate the widespread adoption of MPC in real-world applications.

In this study, we present the design, deployment, and evaluation of an MPC for a dual fuel system. The MPC is designed to eliminate GF usage and thus reduces carbon emissions from heating, through load shifting, achieved by minimizing the electricity cost of the dual fuel system. The control system is based on an algorithm developed in a previous study [17]. The new MPC was deployed in a commercial building served by 5 HPs and 1 GF for 2 months in 2022 winter.

Through this demonstration, this paper provides these three contributions to the literature:

1. A broadly applicable MPC algorithm designed for dual-fuel systems in a SMCB (Section 3)

2. Field implementation and evaluation of this algorithm (Section 4)

3. Lessons learned for the practical implementation of the algorithm and considerations for future deployments (Section 5)

Section 2 presents the demonstration site and the baseline operation of the dual fuel system during a typical day. Section 3 describes the details of the MPC from the building model to the MPC algorithm with experimental schedules. Section 4 shows the experimental results of the dual fuel MPC such as its impact on energy cost, GHG reductions, peak demands, etc. Finally, discussions and conclusions follow in Sections 5 and 6.
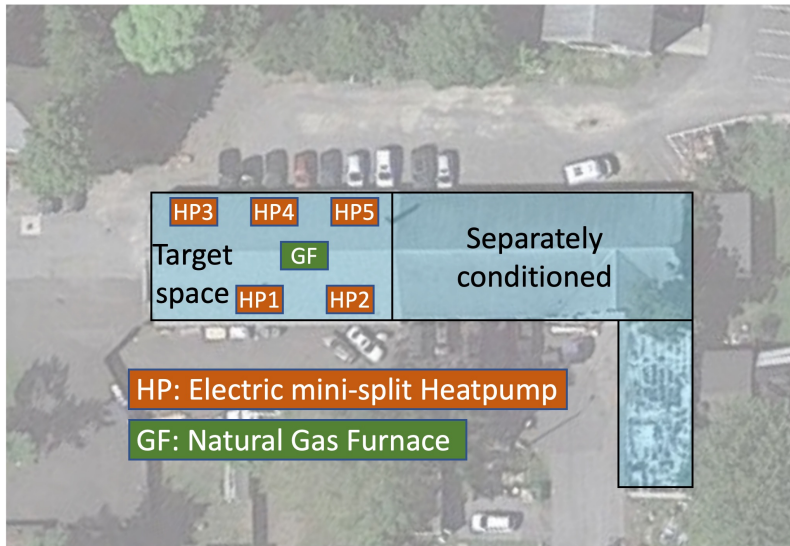
Figure 1: Demonstration site plan: workspaces and HVAC system zones

2. Demonstration site characteristics and baseline operation

2.1. Baseline building and HVAC equipment

The field demonstration site is a small commercial building, located in New York, USA (Figure 1). The building consists of retail, office, and light industrial workspaces, and the actual demonstration was conducted in a single space (approximately 3,780 square feet ($351.2m^2$)), marked as the "Target space" in Figure 1. Originally, this space was conditioned using a GF controlled by a thermostat. In a recent retrofit, five mini-split HPs were installed to reduce gas usage. The HPs were sized to handle the majority of the heating loads and serve as the primary heating source, and the GF was left as a backup heating device. The HPs were manually operated via IR remote controllers and the GF was controlled with a networked thermostat. The interaction of the two systems was managed with a simple control strategy. The heating setpoint for the GF was adjusted to be lower than that of the HPs, guaranteeing activation of the GF in case the heating supplied by the HPs was insufficient, particularly in cold weather conditions. This strategy is commonly known as droop control. The details about the building, HVAC, setpoint schedule, and utility tariff are summarized in Table 1.

2.2. Communication, data collection and control infrastructure

For communication, supervisory control, and data collection, we installed IR transmitters, power meters, and a 4G router connected to the WiFi network as shown in Figure 2. The WiFi-connected IR transmitters (Sensibo Sky[2]) were installed to replace manual IR remote controllers for data collection and supervisory control. The IR transmitters measure room temperatures and send setpoints to mini-split HPs. Those data were sent to the transmitter manufacturer's cloud server via WiFi and were available to us via the cloud server's application programming interface (API). A WiFi-enabled thermostat[3] was already installed on the

---

[2]https://sensibo.com/products/sensibo-sky
[3]https://ecobee.com

Table 1: Building information, HVAC, schedule, and utility tariff summary.

	Description
Target zone information	• Total area: 3,780 square feet ($351.2m^2$). • Spaces: 1 open space with retail and physical work, and 2 private offices. • Glazing: 2'x3' windows (5 in the north and 4 in the south side) and one door on the west side.
HVAC	• HP: 5 Mitsubishi mini-split heat pump (NAX-WPH-15-A112AA). • HP rated capacity[1]: cool 4.4kW, heat 5.2kW, HP rated power[1]: cool 1.4kW, heat 1.5kW. • GF: York/Luxaire (TG8S130D20MP11B) gas furnace (Rated heat 30.4kW).
Default schedule	• HP Occupied: weekday 7:00-20:00, heating setpoint: 21°C, cooling setpoint: 25°C[2] with Fan speed medium. • HP Unoccupied: all time except for occupied time, heating setpoint: 16°C, cooling setpoint: 27°C with Fan speed medium. • GF Occupied: weekday 7:00-20:00, heating setpoint: 19°C[2] for heating with Fan speed medium. • GF Unoccupied: all time except for occupied time, 15°C for heating with Fan Auto.
Utility tariff	Electricity: conEdison General-small Time-of-day (except for June, July, Aug, and Sep). • 00:00-08:00: Off-peak (¢1.38/kWh). • 08:00-22:00 On-peak (¢18.62/kWh). • 22:00-24:00: Off-peak (¢1.38/kWh). Natural gas (con Edison Service Classification No.2). • For the first 88 kWh (or less): \$34.8. • For the next 2549 kWh: ¢3.454/kWh. • For the next 4688 kWh: ¢2.597/kWh. • For the next 8058 kWh: ¢1.715/kWh. • For excess over 8790 kWh: ¢0.883/kWh.

[1] Test conditions are based on AHRI 210/240 [22]

[2] The adjustments of heating and cooling setpoints are limited to 23°C at highest for heating and 23°C at lowest for cooling with 2°C degree deadband..

site, so we simply connected it to WiFi via the 4G router. While HPs and GF-related variables (i.e., zone air temperature (T_{za}), heating setpoint (T_{hsp}), heating operation signal of the GF (u_{GF})) were obtained from the thermostat API, the weather data was recorded via local weather station feed provided by National Oceanic and Atmospheric Administration (NOAA)[23]. The solar irradiance (global horizontal, direct normal, and diffuse horizontal) was estimated by linearly scaling clear sky's solar radiation[24] based on the current cloud cover [23]. In addition, power meters (eGauge[4]) were installed to monitor the power consumption of the HPs. These meters were not required for the MPC but were used for performance evaluation. All the historic data was recorded every 5 minutes, and the weather forecast, including solar radiations, was retrieved in
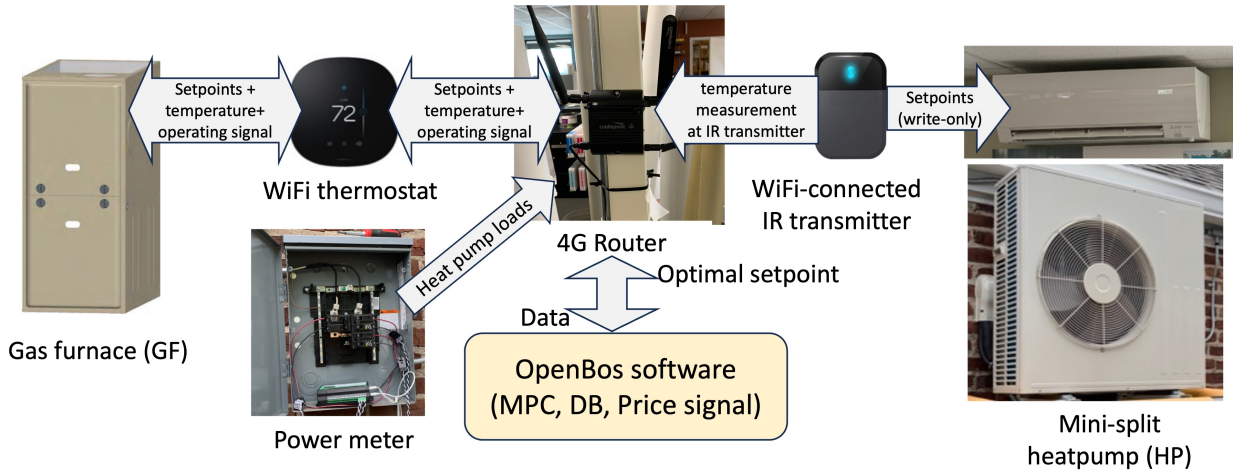
---

[4]https://www.egauge.net/

Figure 2: Schematic diagram of retrofitted IoT devices and power sensors for data collection and control.

real-time via NOAA's API[25].

We used an Eclipse VOLTTRON-based software platform [26], called OpenBOS [27], to integrate all these software interfaces and collect and monitor data, and control its components (Figure 3). OpenBOS is designed to expedite the deployment of advanced control technologies in a scalable manner for SMCBs by allowing the seamless integration of various IoT devices without extensive reprogramming. OpenBOS consists of three layers. The top layer provides portable applications and a dashboard for real-time data monitoring. The portable applications include various control algorithms and strategies including the proposed MPC, that can be easily configured and deployed at multiple sites. The middle layer includes a control, monitoring, and communication middleware, building metadata model (semantic model), and a database. Finally, the bottom layer offers various measurement and control points associated with building systems and external data sources such as weather data and grid price signals. This platform offers several advantages over traditional building automation, including rapid, easy, and cost-effective integration.

However, the use of cloud-based APIs and third-party controllers also had certain drawbacks. High communication latency and intermittent Internet outages, caused by the interaction with the cloud, can reduce the overall performance of the MPC. Additionally, the use of non-conventional IR remote-controlled devices poses a risk of introducing unmeasured variables that can affect the system's operation as a whole. Unlike a standard thermostat, the IR transmitter operates as a one-way communication device, sending only setpoints to the HP (i.e., write-only). In other words, the operating status of the device (the amount of cooling or heating runtime) as well as the temperature measured by the heat pump are unknown (Figure 2). We used the current setpoint and room temperature information to infer the current operational status. This issue is further discussed in the following Section 2.3.

2.3. Baseline building operation

Figure 4 illustrates the baseline operation of the dual-fuel system during a typical heating day. There are six thermostats (five for the HPs and one for the GF), collectively serving six overlapping thermal zones within an open space. The top panel shows the thermostat temperatures of the individual zones and the baseline heating setpoint (Table 1).
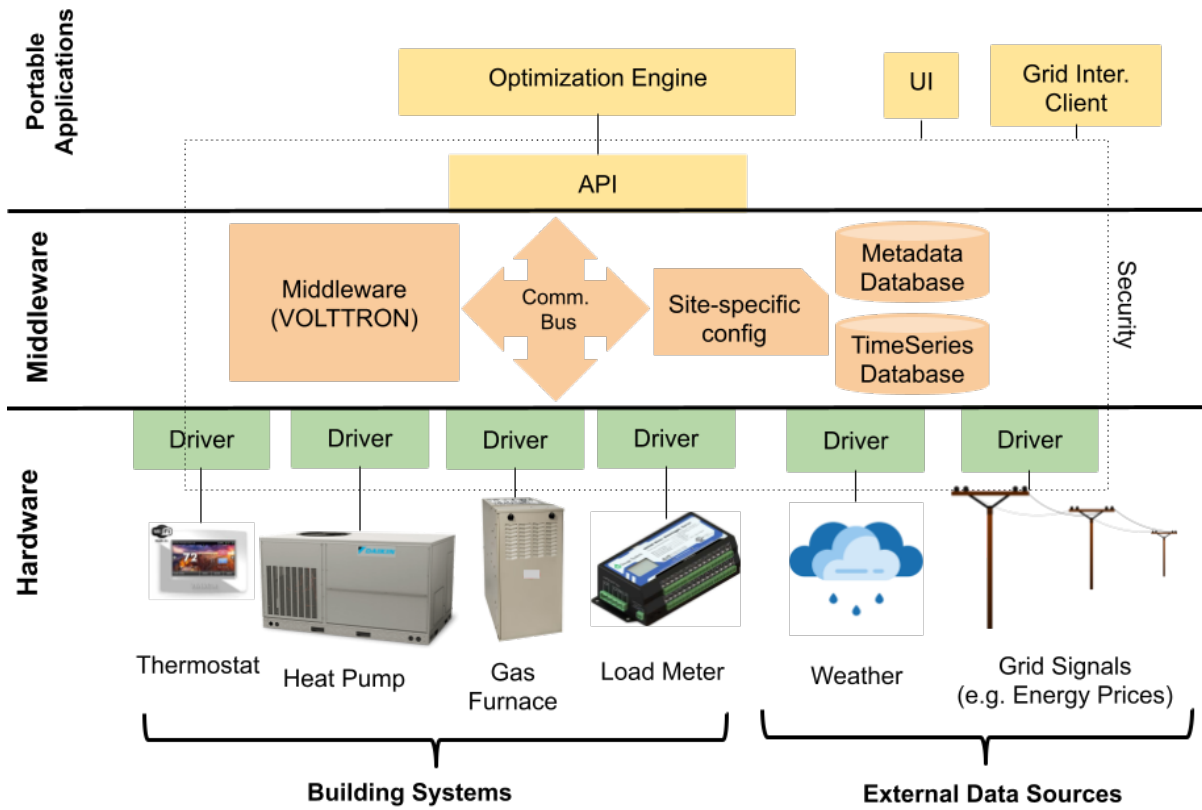
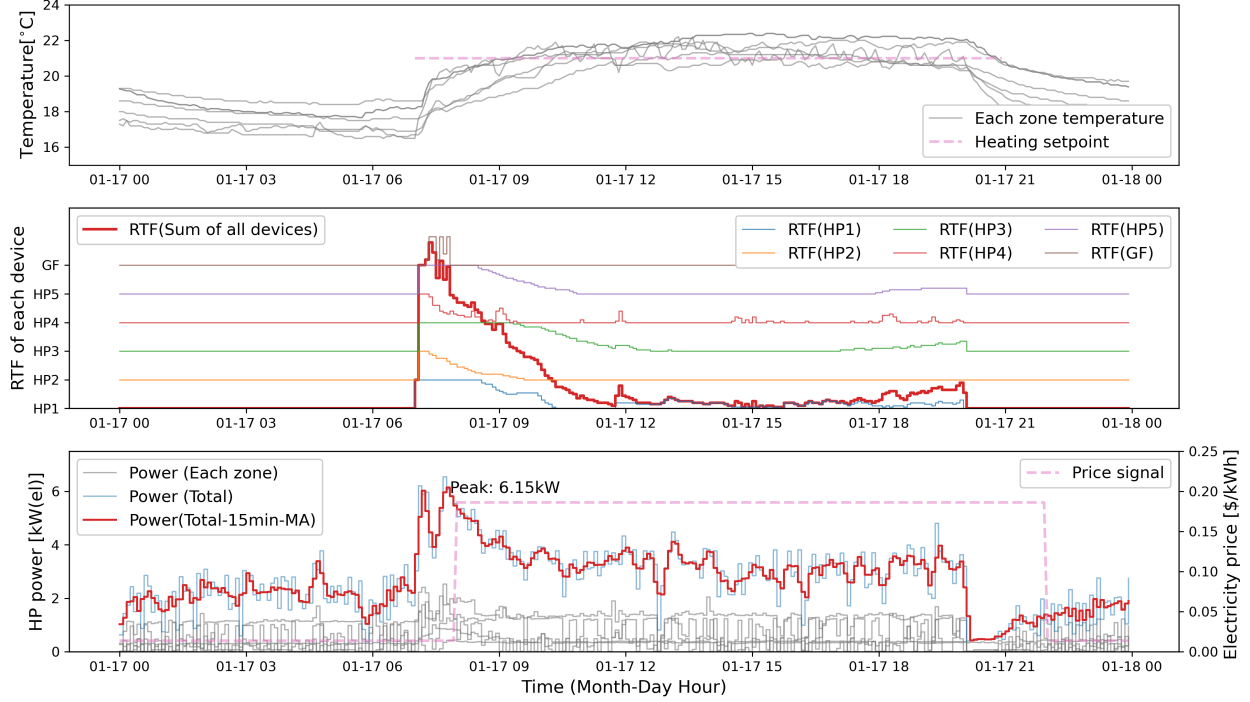Figure 3: Schematic diagram of the software platform.

Figure 4: Illustration of the dual fuel system operation in a typical heating day; Top: temperatures in each zone (grey) and heating setpoint (dotted red); Middle: estimated runtime fraction (RTF) signals of each HVAC unit (colors) and total (bold red); Bottom: HP measured power for each zone (grey), total (blue), total with 15m moving average (bold red) and electricity price signal (dotted pink).

The middle panel depicts the runtime fraction (RTF) of the HPs and the GF heating operation. This value is estimated because the WiFi-connected IR transmitters send setpoints to the HPs in one direction and do not directly report runtime (See Section 2.2). RTFs are estimated using Equation 1 by assuming that the HP compressor signal is proportional to the setpoint error (i.e., $(T_{\mathrm{hsp},i}(k) - T_{\mathrm{za},i}(k))$). K_{p} is set to 0.5 by investigating the HP power data, heating setpoint, and zone temperature during the full load operations.

$$u_{\mathrm{HP},i}(k) = \max[\min[(T_{\mathrm{hsp},i}(k) - T_{\mathrm{za},i}(k))K_{\mathrm{p}}, 1], 0] \tag{1}$$

Lastly, the bottom panel displays both the individual and the total measured power consumption of the HPs, alongside the electricity price signal.

During the night, temperatures gradually decreased, leading to the beginning of heating operations at the start of the occupied period at 7:00. We observe that the cumulative RTF of all devices reached its peak at 7:00, remained high until 8:00 and then gradually decreased. The GF, operating as a backup with a lower setpoint than the HPs (Table 1), was only utilized for a brief period in the early morning. Notably, the power consumption of all HPs peaked at 6.15 kW after applying a 15-minute moving average (which is the typical peak demand charge window). It is worth mentioning that the HPs consumed around 2.5-3 kW even during periods of minimal or no heating operation due to fan functions for air circulation. This pattern
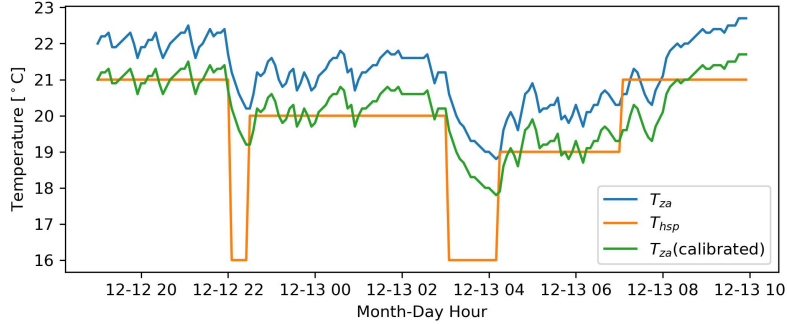
10

Figure 5: Comparison between heating setpoint (T_{hsp}) and transmitter temperature (T_{za}), and the calibrated transmitter temperature (T_{za}(calibrated)). Data analysis shows consistent bias between the last two

was observed consistently throughout the entire day, except during the morning heating period. Considering that the peak pricing period starts at 8:00, there are potential advantages in employing predictive control to initiate heating operations earlier, thereby potentially reducing the need for GF operation while capitalizing on lower electricity rates.

As mentioned in Section 2.2, the IR transmitter does not read the temperature measured by the HP's sensor; instead, it is equipped with its own temperature sensor. Since the HP is controlled based on its own sensor, calibration becomes necessary to approximate the IR transmitter's temperature to the HP's temperature. To perform such calibration remotely and without access to the unit temperature sensor, we intentionally adjusted the heating setpoint over several hours during unoccupied periods. Then, we compared the setpoint and the temperature measured by the IR transmitter and observed that the two temperatures consistently exhibited an offset, as depicted in Figure 5. To realign these variables, we added an offset to the temperature read by the IR transmitter (i.e., $T_{\mathrm{za}} + \text{offset} = T_{\mathrm{za(calibrated)}}$).

2.4. Experimental design

For each day of the experiment (Mid-January-Mid-March 2023), we alternated Baseline or MPC operation. This approach is useful to evaluate the performance of an intervention over the baseline by removing the effect of weather conditions [17], which gives a more fair comparison than the traditional measurement and verification (M&V) procedure During the period, excluding a few days due to network connectivity issues we collected a total of 19 days of Baseline and 13 days and MPC operation, during normal weekdays (i.e., typical business hours), respectively. The key experimental variables are summarized in Table 1.

3. MPC design

3.1. Overview

The MPC algorithm developed in this paper is based on the upper-level MPC (UMPC) procedure presented in [17] applied to dual fuel systems. Figure 6 shows the concept behind this algorithm, hereafter called MPC. Before the beginning of the peak price window, the MPC preheats multiple zones to reduce heating operations when electricity prices are high. It also avoids the simultaneous operation of different units to reduce maximum demand, which would increase electricity bills. Since the original MPC is designed for spaces served by multiple HPs, we treated the GF as a special case of HP for dual fuel MPC. Details of the special treatment are shown in Section 3.3.
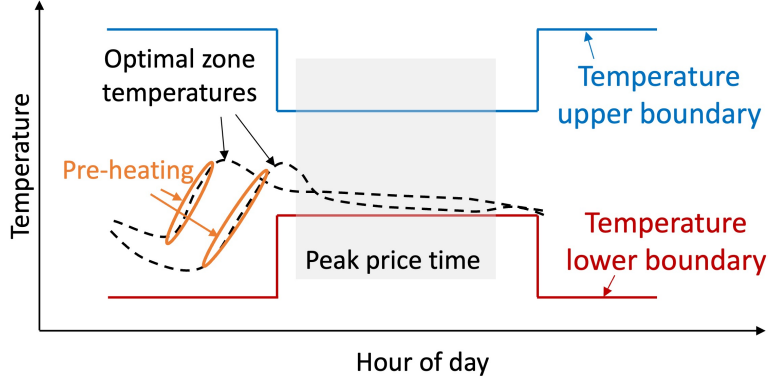
Figure 6: Conceptual diagram of the MPC designed: zones are pre-heated and pre-heating operation is staggered to avoid increasing maximum demand

3.2. Building system model and system identification

A gray-box model structure is widely employed in the field of building controls to predict zone air temperature based on control input profiles and measured disturbances, such as weather forecasts. This approach offers several advantages, including the meaningfulness of each parameter in relation to physical phenomena, the ease of incorporating a priori knowledge regarding the parameters, and the assurance of energy conservation.

System identification (SYSID) in SMCBs is often challenging due to the lack of sensors to capture the presence of unmeasured heat gains such as occupant heat gain, lighting/plug loads, and in/exfiltration. Despite the long history of SYSID research on building applications, studies [28, 29] have shown that the presence of unmeasured heat gains could significantly degrade the performance of SYSID especially when they are correlated with control inputs or measured disturbances regardless of the choices of the model structure and the identification algorithm. However, the installation of additional sensors to measure these unmeasured heat gains might pose an economic challenge and is typically unrealistic for SMCBs. Consequently, our study adopts a specific identification algorithm known as the lumped disturbance (LD) approach, renowned for its robust performance in system identification, particularly when confronted with significant unmeasured disturbances such as occupant heat gains. This article presents a concise summary of the LD approach, while detailed algorithmic descriptions and experimental validations can be found in previous research [28, 29].

In the LD approach, the unmeasured heat gains are modeled as a lumped disturbance term ($\nu(k) := G_{\mathrm{g}}\dot{Q}_{\mathrm{g},1:n}(k)$). Then, it is included in a state-space model as a filtered process of white noise ($G_{\mathrm{g}}\dot{Q}_{\mathrm{g},1:n}(k) = \nu(k) = H(z)e(k)$) as shown in Equation 2.

$$
\begin{aligned}
\mathbf{x}(k+1) &= \mathbf{A}_{\mathrm{d}}(\theta)\mathbf{x}(k) + \mathbf{B}_{\mathrm{d,u}}(\theta)\mathbf{u}(k) + \mathbf{B}_{\mathrm{d,w}}(\theta)\mathbf{w}(k) \quad\quad (2)\\
\mathbf{y}(k) &= \mathbf{C}_{\mathrm{d}}(\theta)\mathbf{x}(k) + \boldsymbol{\nu}(k)\\
\boldsymbol{\zeta}(k+1) &= \mathcal{F}(\rho)\boldsymbol{\zeta}(k) + \mathcal{G}(\rho)\boldsymbol{\epsilon}(k)\\
\boldsymbol{\nu}(k) &= \boldsymbol{\zeta}(k) + \boldsymbol{\varepsilon}(k).
\end{aligned}
$$

The model parameters were estimated using the prediction error method [30, 28]. It provides the parameters that minimize the square sum of one-step ahead prediction error (ε) in Equation 3. The prediction error

is obtained in three steps: innovation calculation (Equation 4), state filtering (Equation 5), and one-step ahead prediction (Equation 6).

$$\theta^*, \rho^* = \arg\min_{\theta} \sum_{k=1}^{N} \left(\boldsymbol{\varepsilon}(k;\theta)\right)^2 \tag{3}$$

$$
\begin{aligned}
\boldsymbol{\varepsilon}(k;\theta) &= \mathbf{y}(k) - \hat{\mathbf{y}}(k|k-1) \\
\hat{\mathbf{y}}(k|k-1) &= \mathbf{C}_{\mathrm{d}}\hat{\mathbf{x}}(k|k-1;\theta) + \hat{\boldsymbol{\zeta}}(k|k-1;\theta)
\end{aligned} \tag{4}
$$

$$
\begin{bmatrix} \hat{\mathbf{x}}(k|k;\theta) \\ \hat{\boldsymbol{\zeta}}(k|k;\theta) \end{bmatrix} = \begin{bmatrix} \hat{\mathbf{x}}(k|k-1;\theta) \\ \hat{\boldsymbol{\zeta}}(k|k-1;\theta) \end{bmatrix} + \begin{bmatrix} \mathbf{0} \\ \mathcal{G}(\rho) \end{bmatrix} \begin{bmatrix} \boldsymbol{\varepsilon}(k) \end{bmatrix} \tag{5}
$$

$$
\begin{aligned}
\hat{\mathbf{x}}(k+1|k;\theta) &= \mathbf{A}_{\mathrm{d}}(\theta)\hat{\mathbf{x}}(k|k;\theta) + \mathbf{B}_{\mathrm{d,u}}(\theta)\mathbf{u}(k) + \mathbf{B}_{\mathrm{d,w}}(\theta)\mathbf{w}(k) \\
\hat{\boldsymbol{\zeta}}(k+1|k;\theta) &= \mathcal{F}(\theta)\hat{\boldsymbol{\zeta}}(k|k;\theta)
\end{aligned} \tag{6}
$$

To represent the building, we developed a six-zone thermal network model to represent six thermostats serving six connected thermal zones in one open space. We used a 2R2C model structure [31] for each zone, and each zone's temperature node ($T_{\mathrm{za},i}$) is thermally connected via thermal resistances. For simplicity of representation, an example model for two of the zones is presented in Figure 7. One can find the detailed notation of the multi-zone structure in [29]. In addition, the incident solar radiation per area on each zone's window ($\dot{q}_{\mathrm{sol,win},i}$) is calculated by using pvlib's plane of array (POA) function[24] from the collected solar radiation data (Section 2.2).

We designed an experiment to perturbate heating setpoints to obtain high-quality data for better SYSID [29] (i.e., uncorrelated control inputs ($\mathbf{u}$), measured disturbance ($\mathbf{w}$), and unmeasured disturbance ($\dot{Q}_{\mathrm{g}}$)). The heating setpoints were perturbated during the 6 unoccupied days (3 weekends) based on a 2-hour time-scale and the 4th order a pseudo-binary random signal (PRBS) [28, 32], which assigned changes in heating setpoints every 2-, 4-, 6-, or 8-hour intervals in random orders to capture the short- and long-term thermal response of the building. The 6 days of data were used to calibrate the building model (Equation 2) for SYSID.

The Scipy [33] nonlinear least-square solver (`least_squares` function) is used to solve the optimization problem of Equation 3. For each weekend data, the initial states (i.e., $\mathbf{x}(0)$) are obtained via a Kalman filter [34] by using the first 6-hours of data. Then, the prediction errors of each weekend are calculated via Equations 4-6, and they are concatenated to a single objective function. To accommodate potential performance variations in ON/OFF heating and cooling operations, the collected data was subjected to a 15-minute moving average. This specific sampling time was chosen to account for the time lag associated with heating and cooling operations (i.e., more than the minimum compressor ON time (5 minutes) while capturing the thermal response of the building [9]).

The optimization was solved 100 times with various initial parameters sampled using the Latin Hypercube Sampling method [35] to avoid local minima. The parameter sampling spaces were chosen based on the physical values with the following rules:

- $C_{\mathrm{w},i}$: [$\tilde{C}_{\mathrm{w,min}}A_{\mathrm{fl},i}th_{\mathrm{min}}$, $\tilde{C}^*_{\mathrm{w,max}}A_{\mathrm{fl},i}th_{\mathrm{max}}$]

13
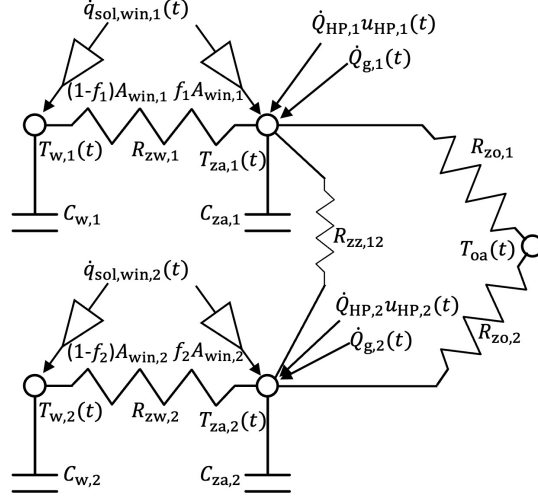
Figure 7: Example case of two-zone gray box model.

- $C_{\mathrm{za},i}$: $[\tilde{C}_{\mathrm{za,min}}A_{\mathrm{fl},i}H_{\min}, \ \tilde{C}_{\mathrm{za,max}}A_{\mathrm{fl},i}H_{\max} \ ]$

- $R_{\mathrm{zw},i}$: $[1/(4(\sqrt{A_{\mathrm{fl},i}})H_{\max}U_{\max}), \ 1/(4(\sqrt{A_{\mathrm{fl},i}})H_{\min}U_{\min})]$

- $R_{\mathrm{zo},i}$: $[1\mathrm{e}\text{-}4, \ R_{\mathrm{zw,max},i}/20]$

- f_i: $[1\mathrm{e}\text{-}9,1]$

- $A_{\mathrm{win},i}$: $[L_{\min}A_{\mathrm{fl},i}, \ L_{\max}A_{\mathrm{fl},i}]$

- $\dot{Q}_{\mathrm{HP},i}$: $[L_{\min}\dot{Q}_{\mathrm{rated,HP}}, \ L_{\max}\dot{Q}_{\mathrm{rated,HP}}]$

- $\dot{Q}_{\mathrm{GF}}$: $[L_{\min}\dot{Q}_{\mathrm{rated,GF}}, \ L_{\max}\dot{Q}_{\mathrm{rated,GF}}]$

-

- ρ_i: $[-0.999,0.999]$

where $A_{\mathrm{fl},i}$: Floor area of ith zone, U: Max. and min. values of U-value [kW/(m²·K)], H, th: Max. and min. values of zone height (H) and thermal mass thickness (th) [m], $\tilde{C}_{\mathrm{w}}$, $\tilde{C}_{\mathrm{za}}$: Max. and min. values of volume normalized capacitance of wall/zone [kJ/(m³·K)], $\dot{Q}_{\mathrm{rated,HP},i}$: Nominal rated heating capacity of ith HP [kW], $\dot{Q}_{\mathrm{rated,GF}}$: Nominal rated heating capacity of GF [kW], L: Max. and min. values of scale variable [-]. The values were chosen based on on-site inspection or general value ranges. Specifically, wind-related values were collected from satellite images and building drawings. The minimum and maximum values of U, H, th, $\tilde{C}_{\mathrm{w}}$, and $\tilde{C}_{\mathrm{za}}$ were decided to $[1 \times 10^{-4}, \ 3 \times 10^{-3}]$[36], [2.0, 5.0], [0.05, 1.0], $[5, \ 3 \times 10^{3}]$[37] and $[1 \times 10^{-5}, \ 5]$[37] according to the ranges typically applicable to a building. The rated heating or cooling rates were based on the rated powers (see Table 1). Lastly, the scale variables ($L_{\min}$: 0.1, and $L_{\min}$: 3.0) were multiplied for the values to get the minimum and maximum boundaries. Because these are different values for each one of the six HPs and it would take too much space to list them all, we only present the

averaged parameter values over the six zones for a reference: C_{w}: 17.0 [kWh/K], C_{z}: 0.32 [kWh/K], R_{zw}: 4.1 [k/kW], R_{zo}: 16.7 [k/kW], f: 0.16 [-], A_{win}: 3.3 [m^2], $\dot{Q}$HP: 3.0 [kW], ρ: 0.99.

To validate the model, we compared temperature predictions with measured temperature profiles on typical unoccupied days (i.e., days not used for training data). Additionally, an alternative validation approach was employed: comparing the estimated RTF with the actual measured RTF. This comparison is critical for MPC because the decision of MPC is the optimal future trajectory of the RTFs of HPs and a GF (i.e., $u_{\text{HP},i}$ and u_{GF}). More details regarding MPC's optimization and control variables can be found in the following Section 3.3.

The estimated RTF ($\hat{\mathbf{u}}(k)$) can be obtained from the measured temperature and the gray-box model through Equations 7 and 8, which is a reformulated version of the state space model (Equation 2). Since all the zones are thermally connected, we estimate the required heating rate of all zones by multiplying the RTF of each zone to the estimated rated heating capacity ($\dot{Q}_{\text{hc},i}$) to make a comparison with the measured data.

$$
\begin{aligned}
\mathbf{y}(k+1) &= \mathbf{C}_{\text{d}}(\theta)\mathbf{x}(k+1) \\
&= \mathbf{C}_{\text{d}}(\theta)\left(\mathbf{A}_{\text{d}}\mathbf{x}(k) + \mathbf{B}_{\text{d,u}}(\theta)\mathbf{u}(k) + \mathbf{B}_{\text{d,w}}(\theta)\mathbf{w}(k)\right)
\end{aligned}
\tag{7}
$$

$$
\begin{aligned}
\hat{\mathbf{u}}(k) &= \left(\mathbf{C}_{\text{d}}\mathbf{B}_{\text{d,u}}(\theta)\right)^{\dagger}\left[\mathbf{y}(k+1) - \mathbf{C}_{\text{d}}(\theta)\left(\mathbf{A}_{\text{d}}\hat{\mathbf{x}}(k) + \mathbf{B}_{\text{d,w}}(\theta)\mathbf{w}(k)\right)\right] \\
\hat{\mathbf{x}}(k+1) &= \mathbf{A}_{\text{d}}\hat{\mathbf{x}}(k) + \mathbf{B}_{\text{d,u}}(\theta)\hat{\mathbf{u}}(k) + \mathbf{B}_{\text{d,w}}(\theta)\mathbf{w}(k)
\end{aligned}
\tag{8}
$$

where † is pseudo-inverse.

3.3. MPC for dual fuel system

The main purpose of the MPC is to minimize the energy cost for a prediction time horizon (e.g., 24 hours) by controlling the setpoints of thermostats. The control problem of the MPC for multiple HPs and a GF at time k can be written as Equation 9.

$$
\begin{aligned}
\min_{\substack{\bar{u}_{\text{HP},i}(j),\bar{u}_{\text{GF}}(j)\in\mathbb{R},\\ \delta,\Gamma_{\text{l},i},\Gamma_{\text{u},i}\in\mathbb{R}^{+}}} \quad & \sum_{j=1}^{N_p}\sum_{i=1}^{n}\left[\begin{array}{l} ER_{\text{el}}(k+j-1)P_{\text{HP},i}(k+j-1)\bar{u}_{\text{HP},i}(k+j-1)+ \\ ER_{\text{ng}}(k+j-1)P_{\text{GF}}(k+j-1)\bar{u}_{\text{GF}}(k+j-1)+ \end{array}\right] + \\
& \omega_{\text{d}}\delta + \omega_{\text{l}}\Gamma_{\text{l}} + \omega_{\text{u}}\Gamma_{\text{u}} \\
\text{s.t.} \quad & T_{\text{l},i}(k+j) - \Gamma_{\text{l}} \le \hat{\bar{y}}_i(k+j)|k \le T_{\text{u},i}(k+j) + \Gamma_{\text{u}} \,(\forall i \in \{1,\cdots,n\} \\
& \sum_{i=1}^{n}P_{\text{HP},i}(k+j-1)\bar{u}_{\text{HP},i}(k+j-1) \le \delta \\
& 0 \le \bar{u}_{\text{HP},i}(k+j-1) \le 1 \,(\forall j \in \{1,\cdots,N_{\text{p}}\}) \\
& 0 \le \bar{u}_{\text{GF}}(k+j-1) \le 1 \,(\forall j \in \{1,\cdots,N_{\text{p}}\})
\end{aligned}
\tag{9}
$$

where j is the control timestep from the current timestep k, i is the index of HP device, ER is electricity cost rate [\$/kWh], $\bar{u}_{\text{HP},i}(k+j)$ and $\bar{u}_{\text{GF}}(k+j)$ are the HPs and GF heating RTFs for the averaging window for the ith unit at the $(k+j)^{th}$ timestep of the MPC and optimization variables, $\hat{\bar{\mathbf{y}}}(k+j)|k$ is the j-step temperature prediction via the building model (Equation 10) given the historic data ($\cdot|k = \{\bar{y}(k-1), \bar{y}(k-$

2), $\cdots$, $\bar{u}(k+j-1), \bar{u}(k+j-2), \cdots$}), $(T_{l,i}(k+j), T_{u,i}(k+j))$ are the desired heating and cooling setpoints for i^{th} HP, $\omega_l, \omega_u(\in \mathbb{R}^+)$ and $\omega_d(\in \mathbb{R}^+)$ are weights on variables of $\Gamma_l, \Gamma_u(\in \mathbb{R}^+)$ and $\delta(\in \mathbb{R}^+)$, δ is an optimization variable for peak demand, Γ_l and Γ_u are optimization variables for comfort violation.

$$\hat{\bar{\mathbf{x}}}_a(k+j+1|k) = \mathbf{A}_a\hat{\bar{\mathbf{x}}}_a(k+j|k) + \mathbf{B}_{a,u}\bar{u}(k+j) + \mathbf{B}_{a,w}\bar{\mathbf{w}}(k+j)$$
$$\hat{\bar{\mathbf{y}}}(k+j|k) = \mathbf{C}_a\hat{\bar{\mathbf{x}}}_a(k+j|k) \qquad (\forall j \in \{1, \cdots, N_p\})$$
$$(10)$$

where $\hat{\bar{\mathbf{x}}}_a(k)|k$ are the filtered states at the current time k with historic data via Kalman filter on the augmented model (Equation 11) [38, 39]. This offset-free MPC is used to remove the steady-state errors from unmeasured disturbances [40]. In Section 5 we discuss the limitations of this method and the impact of unmeasured disturbances on future predictions.

$$\mathbf{A}_a = \begin{bmatrix} \mathbf{A}_d(\theta^*) & \mathbf{A}_{ud} \\ \mathbf{0} & \mathbf{0} \end{bmatrix}, \ \mathbf{B}_a = \begin{bmatrix} \mathbf{B}_d(\theta^*) \\ \mathbf{0} \end{bmatrix} \ \mathbf{C}_a = \begin{bmatrix} \mathbf{C}_d(\theta^*) \\ \mathbf{0} \end{bmatrix}^T \ \hat{\bar{\mathbf{x}}}_a = \begin{bmatrix} \hat{\bar{\mathbf{x}}} \\ \boldsymbol{\zeta} \end{bmatrix} \ \mathbf{A}_{ud} = \begin{bmatrix} \mathbf{0} \\ \text{diag}(\frac{1}{C_{za}^*}) \end{bmatrix} \qquad (11)$$

where $\boldsymbol{\zeta}$ is unmeasured disturbances of zones as input disturbances format (i.e., heat gain).

The control problem in Equation 9 provides the optimal sequence of RTFs for HPs and a GF to minimize the total energy cost given the constraints. However, the optimization problem is slightly modified to meet the customer's goal, whch reduces the use of the GF heating as much as possible for electrification and decarbonization. To achieve this, we treated the GF as a special type of HP with very low efficiency (i.e., very high power consumption) that is only used when there is the risk of temperature violations. Specifically, P_{GF} is set to $w_l/ER_{el,offpeak}$ and ER_{ng} is set as same with ER_{el}. With this weight, the GF is used in addition to the HPs if there is a temperature violation of 1°C or more when using only the HPs during the offpeak hours.

A critical design consideration here was that modeling COP requires additional sensors, including individual power meters. This entails increased costs for sensor installation, communication, and commissioning, making it cost-prohibitive when dealing with a large number of small HVAC units (which is not scalable). To promote scalability we came up with a simplified approach that neglects the impact of COP with respect to changes in outdoor air temperature and other factors (note that we used the nominal rated power scaled by the RTF for each unit in the objective function). We acknowledge that this approach may not be useful for energy-efficiency maximization scenarios, which require better knowledge of the COP for each unit. However, for the electricity-cost optimization problem, the constant power approach could yield a decision close to optimal, especially when the variation in utility cost rates is larger than that of the COPs. This is because, in the electricity-cost minimization problem, the weight assigned to each optimization variable (RTF in our case) includes the electricity rate, not just power or COP.

(Table 2) shows the relationship between heating capacity and outdoor air temperature, based on the manufacturer's data. The heating capacity does not change with outdoor air temperatures between 10°C and -15°C. The HPs likely have an internal logic to provide a consistent heating capacity over that temperature range, which presumably follows the design requirement of the DOE's Residential Cold-Climate Heat Pump Technology Challenge [41], which requires the minimum ratio of maximum heating capacity at -15°C to the nominal capacity at 8.3°C equal to one. It decreases to 90% and 81% when the outdoor air temperatures are -20°C and -25°C, respectively, and the operation of HPs is prohibited under -25°C. To encode the shutoff threshold of the HPs during the cold weather in MPC, we increase the values of ER below the threshold so that the multiplication of $ER \times P_{HP}$ increases in Equation 9 (i.e., HP usage is not used when ER is high) to simplify data processing. In addition, we use a very high number when the outdoor air temperature is lower

than the threshold (-25°C) to prevent the use of HPs. On the other hand, GF's operation is not directly related to the demand term (δ in Equation 9), so we set the $P_{\mathrm{HP},i}$ of GF as 0 for the calculation of the demand term. ω_l, ω_u and ω_d are set to 1000, 1000, and 10. δ is set to 70% of the summation of all HP powers.

Table 2: Heating capacity of the heat pump, based on manufacturer's data.

Outdoor temperature [°C]	Heating capacity [kW]	Percentage of rated capacity [%]
10	5.28	100%
5	5.28	100%
0	5.28	100%
-5	5.28	100%
-10	5.28	100%
-15	5.28	100%
-20	4.75	90%
-25[1]	4.27	81%

[1] Below this temperature, the heat pump should not be used.

Once the optimal RTFs of HPs an GF ($\bar{u}^*_{\mathrm{HP},i}(k)$ and $\bar{u}^*_{\mathrm{GF}}(k)$) at current time k are calculated by the optimization process (Equation 9), the optimal heating setpoints are decided through Equation 12. Specifically, when the optimal RTFs of HPs and GFs are non-zero (i.e., heating is required for that zone), the corresponding next-time temperature predictions ($\hat{\bar{y}}_i(k+1|k)$) are used for the optimal heating setpoints of the thermostats. Otherwise, the baseline heating setpoints are assigned to the thermostats.

$$
\begin{aligned}
T^*_{\mathrm{hsp},i}(k) &= \left\{ \begin{array}{ll} \hat{\bar{y}}^*_i(k+1|k), & \text{if } \bar{u}^*_{\mathrm{HP},i}(k) > 0 \\ T_{\mathrm{l},i}(k), & \text{if } \bar{u}^*_{\mathrm{HP},i}(k) = 0 \end{array} \right. \\
T^*_{\mathrm{hsp,GF}}(k) &= \left\{ \begin{array}{ll} \hat{\bar{y}}^*_{\mathrm{GF}}(k+1|k), & \text{if } \bar{u}^*_{\mathrm{GF}}(k) > 0 \\ T_{\mathrm{l,GF}}(k), & \text{if } \bar{u}^*_{\mathrm{GF}}(k) = 0 \end{array} \right.
\end{aligned}
\tag{12}
$$

The MPC is a mixed integer linear problem and is solved by using `pyglpk` Python package [42]. The MPC's sampling time (i.e., control cycle) is set to 15 minutes, the same as the HP RTF's sampling time (Section 2.3).

4. Results

4.1. System identification result

Figure 8 depicts a comparison between the predicted and measured values of the building model using test data. The upper panel in Figure 8 (a) illustrates the temperature predictions for a single zone, while the middle panel shows the corresponding inputs such as control RTFs and solar radiation. The bottom panel of Figure 8 (b) shows the comparison of the estimated and measured required heating for all zones (as outlined in Equations 7-8). Overall, the predicted temperatures displayed reasonable alignment with the measured data, exhibiting a root mean square error (RMSE) of 0.42°C. The predictions effectively captured the thermal response of the zone, except for instances of abrupt temperature drops or rises, which could be attributed to transitions from occupied to unoccupied modes, or unmeasured human- or device-induced heat gains. The estimated required heating shows a jagged profile including negative values. The negative
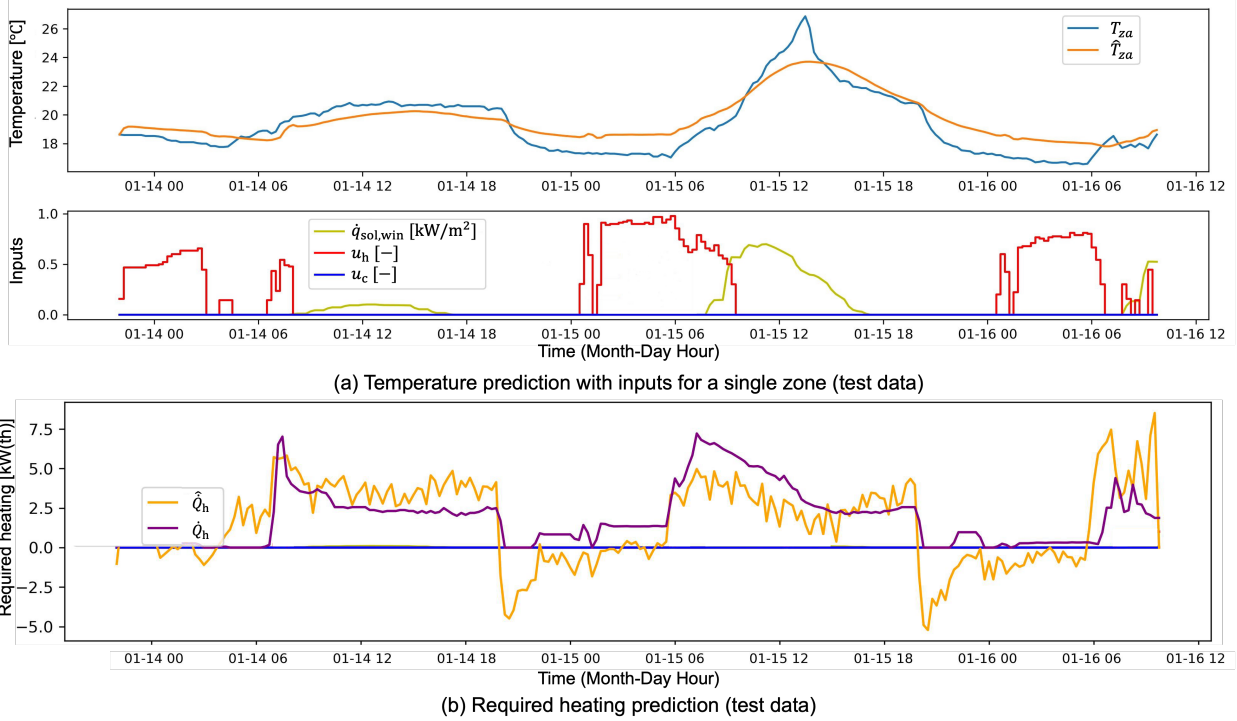
17

Figure 8: Comparison of predicted (or estimated) and measurement values of the building model on test data: (a top) single-zone temperature (a bottom) inputs and (b) required heating rate for the space.

values can be interpreted as a need for cooling to meet the exact measured temperature at the timestep. This is typically not real cooling but is observed due to sudden temperature fluctuations. Those noisy or negative values were mainly observed during the transition time between occupied to non-occupied times due to the sudden temperature variations from device shut-off. Small discrepancies are attributed to unmeasured disturbances such as infiltrations. Despite those discrepancies, the estimated values effectively capture the general pattern of the measured heating requirements, especially during the occupied heating times.

4.2. Day-by-day comparison

For the purpose of the day-to-day comparison shown in Figure 9, representative winter days featuring typical cold conditions were selected for both the Baseline and MPC scenarios. In the Baseline case (Figure 9 (a)), the HPs primarily showed fan operations (remaining always-ON) during the early morning period, with heating operations starting around 7:00 and achieved setpoints by approximately 9:00-10:00. Due to all HPs being activated during the morning heating period, the electricity demand reached its peak demand, 6.52 kW around 8:00. Additionally, although not visible in this figure due to space constraints, the GF was operational for approximately 40 minutes.

In contrast, the MPC strategy initiated pre-heating operations near 3:00 to smooth the morning heating demand. Consequently, the peak electricity demand was reduced to 5.6 kW, and no GF operation was required. It is worth noting that while the measured room temperatures exhibited some uncertainty in
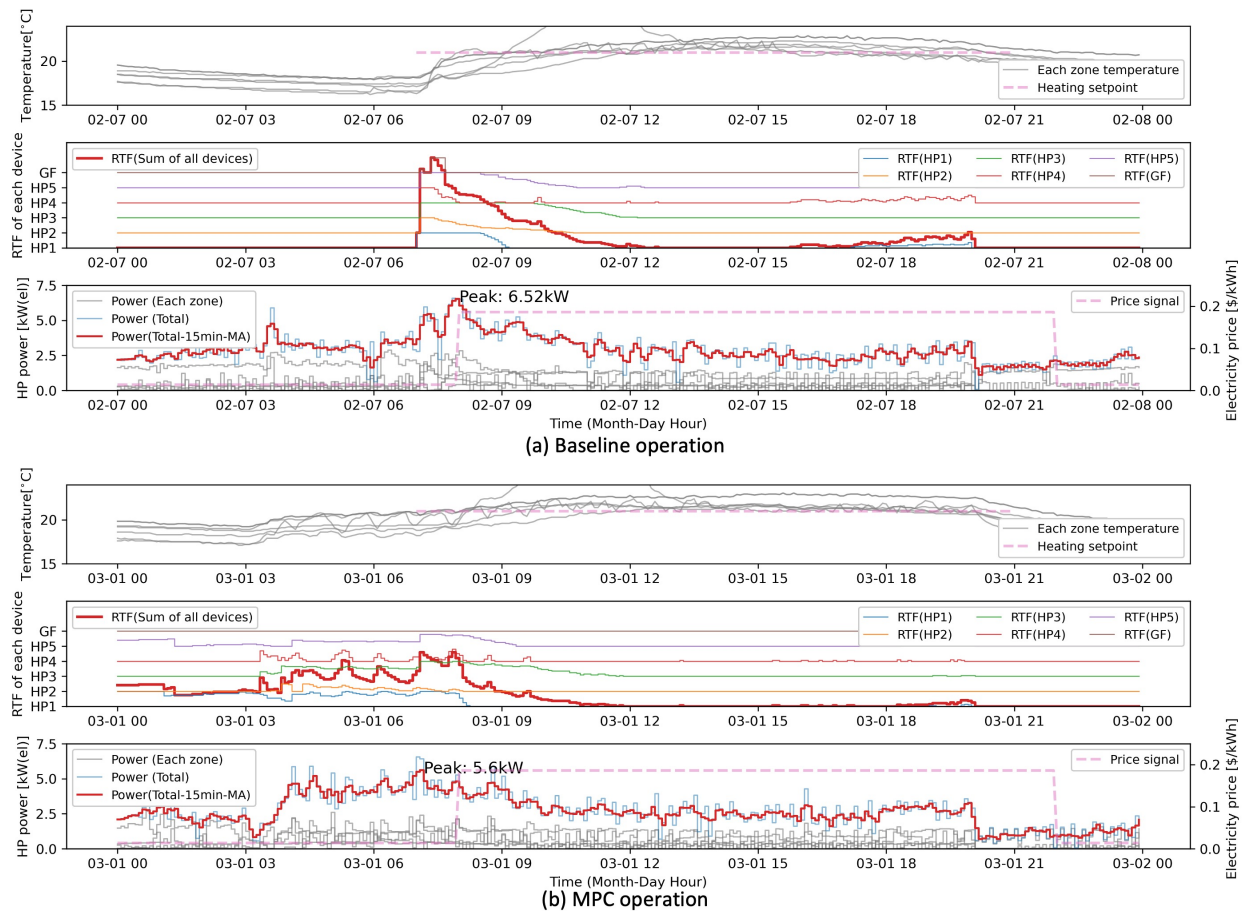
Figure 9: Comparison between Baseline and MPC using data from similar days.

comparison to the HP temperature sensors, the temperature profiles generated by MPC showed similar trajectories to those observed in the Baseline scenario during occupied hours, as discussed in Sections 2.2-2.3.

4.3. Load Shifting, peak demand and hourly operation summary

Figure 10 presents a comprehensive comparison between average daily profiles of mechanical heating rates (Top) and average daily profiles of outdoor air (Bottom) profiles of the Baseline and MPC scenarios across all experiment days. For this comparison, the mechanical heating rates are calculated by multiplying the nominal rated heating capacity of the HP and GF by their RTFs because the mechanical heating rates were not directly measured.

Each day's mechanical heating rate is depicted as faintly colored lines, while the average profiles for all days are represented by a bold line. In addition, the electricity cost is displayed on the right-hand side y-axis. It's worth noting that the building's occupied schedule started at 7:00, resulting in the MPC effectively
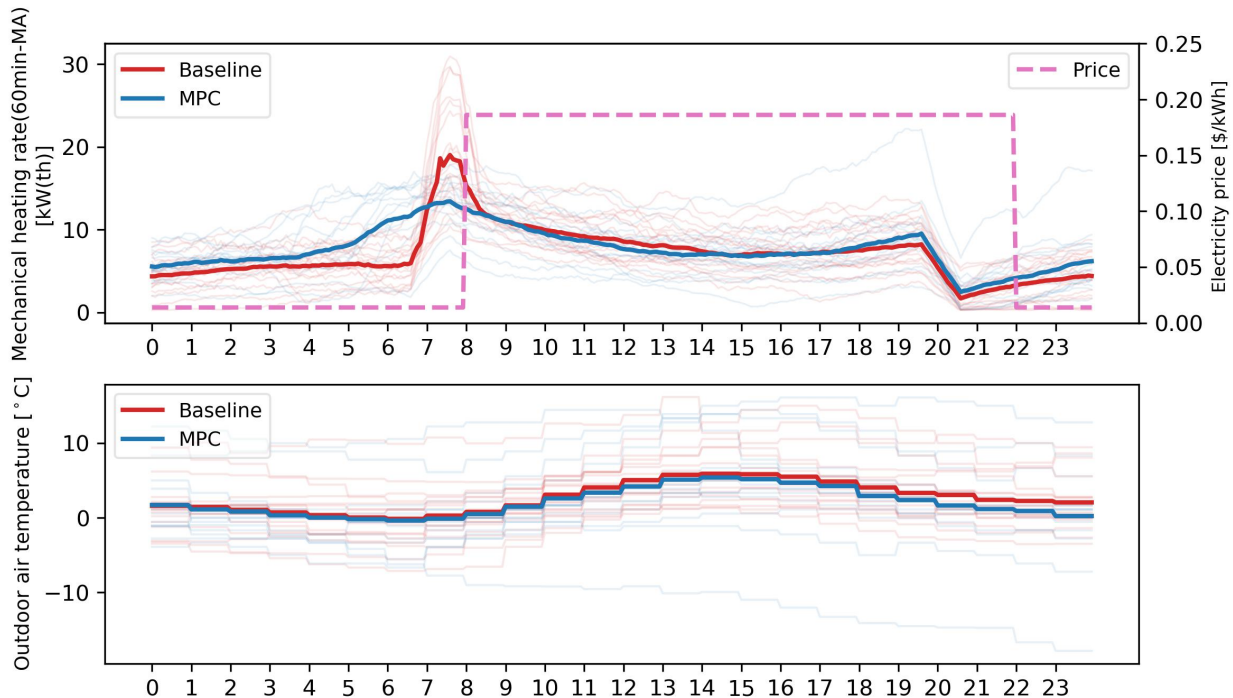
Figure 10: Comparisons of average daily profiles of mechanical heating rates (Top) and average daily profiles of outdoor air (Bottom) between Baseline and MPC days; dimmed profiles indicate each daily profile

avoiding ToU peak hours. In contrast, the Baseline control strategy demonstrates a morning heating peak that occurs between 7:00 and 8:00.

The essence of the MPC's design, centered around load shifting, becomes evident as it successfully relocates the peak thermal load to the early morning hours. This results in smoother thermal load profiles and consequently a significant 23% reduction in thermal load during 7:00-8:00 when compared to the Baseline.

Figure 11 presents the comparison of daily electric peak load of HPs for all days. The objective function (Equation 9) takes into account the daily peak load of HPs, but it only considers peaks within the day's prediction horizon, allowing some flexibility in the regulation of the absolute value of monthly peak demand within the MPC. Despite this limitation, the MPC still achieves a 14% reduction in electricity peak demand of HPs through effective load shifting, even without using GF for heating at all. However, it is worth noting that peak demand can be influenced by the number of operating HPs, leading to higher peaks on certain MPC days, especially during defrost cycles or when small heating loads are involved as the demand term is designed to limit the demand to 70% of total HP power (Equation 9 and Section 3.3).

Overall, the zone temperatures during MPC operation were higher than those on Baseline days during unoccupied times. However, indoor temperatures were also slightly higher during MPC days in occupied periods, resulting in lower HP electricity consumption. This reduction in consumption is the desired outcome of MPC and is likely the result of stored heat in the building's thermal mass through unoccupied time heating. This remains a hypothesis, since we did not set up sensors to measure temperatures inside the
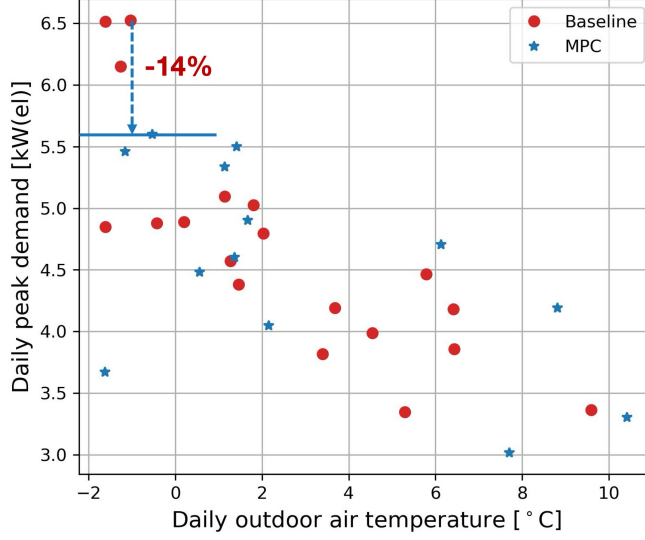
Figure 11: Comparison of daily electric peak load of HPs between Baseline and MPC days.

building envelope and other thermal masses. One may notice that the temperature increase at 7 AM is much higher in the Baseline despite similar HP electricity consumption. This is attributed to the use of the GF during this time, as shown in Figure 12.

4.4. Electricity, cost, and gas use reduction

Figure 13 provides a comprehensive summary of electricity usage, electricity cost, and GF usage hours during demonstration periods. To account for variations in outdoor air conditions, we used the change-point model [43] for evaluation, and their confidence intervals were obtained by linear regression as shown in Equation 13 [44].

$$\hat{E}_j \pm t_{\alpha/2,n-2}\sqrt{\frac{\sum_{i=1}^{n}(E_i - \hat{E})^2}{n-2}}\sqrt{\frac{1}{n} + \frac{(T_{\text{oa,day},j} - \bar{T}_{\text{oa,day},1:n})}{\sum_{i=1}^{n}(T_{\text{oa,day},i} - \bar{T}_{\text{oa,day},1:n})^2}} \tag{13}$$

where E is daily electricity consumption [kWh/day], j is the index of grid points where the confidence intervals are estimated, $t_{\alpha/2,n-2}$ is t-statistic of confidence interval level (α=0.95),n is the number of data points for the change-point model, i is the index of data points 1, 2, ... , n, $T_{\text{oa,day}}$ is daily mean outdoor air temperature.

Both the MPC and Baseline exhibit similar electricity consumption, resulting in an overlap in the confidence interval of change-point models. This overlap can be interpreted as indicating no statistical differences between MPC and Baseline, and vice versa. This outcome is anticipated, given that MPC didn't engage the GF at all, in contrast to the Baseline where it was active for a brief duration (less than an hour per day), as seen in the right-side figure. It should be noted that the daily heat pump usage ranges from 120 to 280 kWh, based on the rated values of COP (Section 2.2), while 0.3 hours of gas furnace operation involves approximately 10 kWh of heat, a value smaller than the confidence intervals.
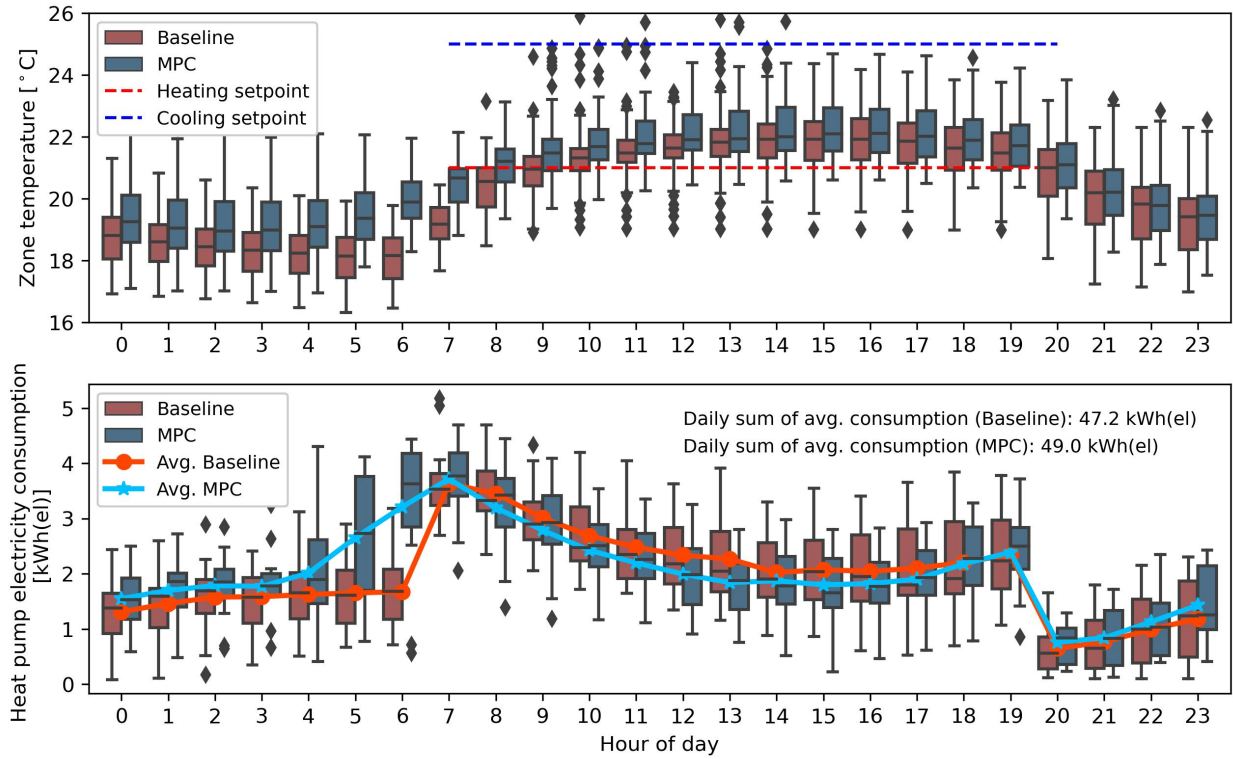
21

Figure 12: Comparisons of hourly temperature distributions of all thermostats (Top) and hourly electricity distributions of all heat pumps (Bottom) between Baseline and MPC days; line profiles indicate average hourly electricity consumption
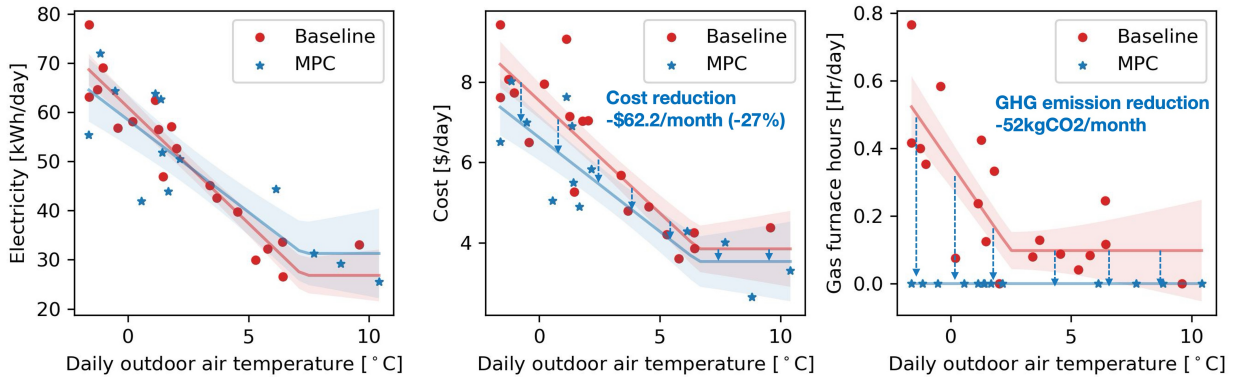
Figure 13: Summary of electricity usage, electricity cost, and GF usage hours in all experiment periods

Moving to the middle plot, it becomes evident that MPC strategically achieved lower energy costs by preheating during off-peak hours, yielding a reduction of $62.2/month (27%). This reduction was mainly due to the decrease in fixed natural gas costs (as outlined in Table 1). It's worth noting, however, that if peak pricing times (beginning at 8:00) align with peak demand times (between 7:00 and 8:00), the potential for savings could be further enhanced. Moreover, while the weather became mild, the pre-heating period naturally shortened, leading to diminished cost differences.

Furthermore, MPC entirely avoided the use of GF and successfully reduced GHG emissions by approximately 52kgCO2 per month, as calculated using simple GHG equivalencies calculator [45]. Note that this reduction only accounted for a decrease in GF usage, as there was no significant reduction in daily electrical consumption, which is not included in the objective function but is a byproduct of the optimization.

Finally, Tables 3, 4, and 5 present the infrastructure costs for MPC, implementation time for MPC, and infrastructure costs for M&V, respectively. The cost of the MPC control infrastructure, including devices and installation, amounted to $975 . Based on the cost information and the assumption that the WiFi infrastructure is already established on the site (i.e., no requirement of $110/Month for cellular modem and data service), the capital costs would be paid back in approximately 13 heating months. In addition, we also estimated the approximate time cost for MPC implementation. Building metadata creation from drawings (e.g., floor area of thermal zones and locations of sensors and HPs) and sensor data connection to OpenBOS software take up the majority of the time. Once it is all configured, the data commissioning, design of experiments, and modeling of the building take 1 or 2 days for each task because they are already automated. However, as stated in Section 2.2, the estimates do not take into account the time for implementing the MPC, because the same algorithm can be reused across sites. Finally, the majority of hardware costs were infrastructure costs for M&V. Each unit was individually metered to improve M&V for research purposes. This metering is not required for the operation of the MPC and thus may not be required for future implementations.

5. Discussions, limitations and future works

Factors affecting the results

23

Table 3: Infrastructure costs for MPC [Hardware]

Category	Item	Cost
Labor	Estimated MPC infrastructure installation	$320
Equipment	Smart thermostat	$205
	HP controllers	$450
Totals	Capital and labor cost for MPC control infrastructure	$975

Table 4: Implementation time for MPC

Category	Task	Time required
Labor	Building metadata creation from drawing	3 [day]
	Sensor data connection to OpenBOS software	4 [day]
	Data commissioning for the 6 thermostats	1 [day]
	Design of Experiments (setpoint perturbation test)	1 [day][1]
	Model building and validation for 6 units	2 [day]

[1] This one-day period is the time required for defining and programming the thermostat setpoint schedule for all thermostats. Once coded, the schedule was automatically implemented over eight weekend days for data collection.

Table 5: Infrastructure costs for M&V

Category	Task	Cost
Labor	Scoping	$2000
	Estimated metering installation	$2720
	Commissioning and hand-off	$800
Equipment	Cellular modem and data service	$110/Month
	Meters	$1700
	Miscellaneous	$110
Totals	Capital and labor cost for metering for M&V	$7330

The proposed technology achieved significant energy cost saving (27%) and load shifting (23%) performances during the two winter months of field testing. During the test periods, the daily mean outdoor air temperature ranged from -2°C to 11°C, which corresponds to the typical weather range (from -2.3°C to 9.9°C) during Dec-Mar of the site location (New York area in U.S.)[46] though there were no extreme cold weather days during the experiment. We believe similar performance should be expected in other buildings in the same climate zone, but we acknowledge that to generalize these results rigorously, additional field-work is required. Savings may also vary based on climate zones, building types, and occupancy patterns.In addition, the price signal also plays an important role. As shown in Figure 10, the peak price time starts at 8 AM, but the HVAC occupied hours start at 7 AM. Considering that the morning peak demands typically happen around 7-8 AM, more energy cost savings and improved load shifting performance can be achievable if the occupied peak and electric price time overlap.

Applicable system

The MPC was applied for a dual fuel system that is composed of separate HPs and GF equipment. Such a setup is often found in the HP-retrofitted existing SMCBs. It is important to note that the proposed MPC is specifically designed for this type of HP + GF system. Some companies offer factory-packaged dual fuel systems that are not compatible with the MPC presented in this paper because control algorithms for these systems are typically designed by the device manufacturer and embedded in the hardware without allowing for external modifications. However, our MPC could be easily modified if the manufacturer provides an API to directly control the separate components of the package system. For this reason, having interoperable interfaces for packaged systems would allow to develop and test a multitude of algorithms with different objective functions, ranging from limiting GF usage to reducing energy costs and curbing GHG emissions.

IR transmitter and data uncertainty

One of the main limitations of this study is the low data quality due to the use of 3rd party IR transmitters (Figure 2). Traditionally, the ON/OFF HP unit is controlled by a standard thermostat. In this case, the HP is controlled by the temperature measurement (i.e., measured process variable) of the thermostat, so good quality temperature measurements and HP's operating signals are available except for any sensor uncertainty.

However, the scenario changes with mini-split HPs, which have gained popularity in SMCBs owing to their heightened efficiency and ease of installation. These units are often controlled by an IR remote controller [7]. Due to the different communication interfaces between different manufacturers, the WiFi-connected IR-transmitter is a practical option for a low-cost interface for supervisory control. As discussed in Sections 2.2-2.3, both the measured process variable (i.e., room temperature reading for mini-split HP) and the operating signals are indirectly obtained from the estimation. This, in turn, amplifies the need for engineers to invest more effort in commissioning and troubleshooting the supervisory control.

Nevertheless, the results of this study still underscore the merits of the MPC approach. However, this situation once again highlights the importance of standardized and interoperable systems across various HVAC configurations (e.g., ON/OFF HPs, mini-split HPs, packaged dual-fuel HPs, etc.). Such standardization would enable the rapid scaling of the innovative optimization algorithm and accelerate national decarbonization efforts.

Model for the HP

As discussed in Section 3.3, designing the MPC model for the HP involves various considerations due to the trade-off between accuracy and practicality. We want to have a model that provides sufficient accuracy, without being too complex. Increasingly complex models may necessitate larger datasets for training, and more expensive optimization solvers, and may also require additional sensors and labor for installation. In consideration of these factors, we designed the system as described in Section 3.3..

However, it is important to understand when the proposed model is applicable and what its limitations are. The proposed optimization model structure can be easily extended to a linear performance map model as

25

a function of outdoor air temperature (i.e., a mixed-integer linear problem), while a more complex structure, such as the inclusion of chilled water supply temperature or indoor wet-bulb temperature, requires a non-linear optimization solver. The use of these performance maps is typically beneficial when the overall efficiency of the HVAC system is the primary target and these variables are controllable. However, RTUs in SMCBs are very simple, and our approximations of the HP performance models are practically reasonable as we observed from the performance improvement of the MPC operation in comparison to the Baseline.

Building model

While using a simplified MPC model has hardware cost and labor benefits, this approach introduces substantial technical hurdles in both modeling and control. To tackle these challenges, this study employed the lumped disturbance system identification algorithm and the offset-free MPC method. They integrate explicit models of unknown disturbances and are underpinned by robust theoretical foundations. Nevertheless, these approaches demonstrate constrained performance, especially for the long-term time scale, which demands a high-quality model in a low-frequency domain. From two perspectives, these prediction errors are inevitable in this type of practical solution. First, it is necessary to have the future disturbances information for accurate prediction (regardless of the accuracy of the building thermal model), but they are not typically measured within the control framework. Also, asymptotic model errors can occur when the data period that is used for model training is affected by dominant unmeasured disturbances, and they are correlated with other data inputs regardless of the system identification methods or model structure [29]. Finally, the inclusion of a model for stochastic future unmeasured disturbance is a still research area whose impacts are already included in the gray-box model and offset-free MPC in a short time scale [39].

6. Conclusion

This paper presents a demonstration of MPC geared towards optimizing the operation of HPs and GF dual-fuel systems in SMCBs. The MPC design leverages cost-effective sensing and actuating devices, showcased through a real-world application in an office building with five HPs and a GF, spanning a 2-month duration.

The test results clearly demonstrate the effectiveness of the MPC, showing a 27% reduction in costs and the complete elimination of GF usage. This reduction is achieved by strategically shifting 23% of the thermal load from occupied-peak hours to non-occupied-non-peak hours. Furthermore, the adoption of the MPC translates into a noteworthy monthly reduction of 52 kgCO2 of GHG emissions, via a simple equivalency calculation. While this study did not incorporate electricity marginal emissions signals, their inclusion could potentially yield even more aggressive GHG reductions, particularly on the HP front.

In summary, the outcomes emphasize the considerable potential of MPC-based optimization for dual-fuel systems in SMCBs, delivering cost savings, minimized GF usage, and substantial reductions in GHG emissions. Among 5.6M SMCBs ($\leq 50,000$sqft ($4,645$m^2)) in the U.S., 50% of them have non-electric heating devices as a main source of heating [47], so the potential of this technology is tremendous with the rising demand of electrification. However, limitations remain, especially concerning data quality and model uncertainty, stemming from non-interoperable communication services (such as the IR remote controller) within the practical MPC structure. Therefore, the future calls for enhanced efforts from both industry and academia, focusing on both hardware (such as interoperable controllers) and software (to enhance MPC system performance).

7. Acknowledgements

References

[1] L. Paul, S. Ham, M. Pritoni, D. Kim, R. Brown, J. Feng, Field implementation of MPC for heat Pump-Based duel fuel systems in small commercial buildings for decarbonization, in: 2023 ASHRAE Annual Conference at Tampa, FL, 2023.

[2] P. Jadun, C. McMillan, D. Steinberg, M. Muratori, L. Vimmerstedt, T. Mai, Electrification futures study: End-use electric technology cost and performance projections through 2050, Tech. Rep. NREL/TP-6A20-70485, National Renewable Energy Lab. (NREL), Golden, CO (United States) (2017). doi:10.2172/1416113.

[3] P. Glanville, M. Mensinger, Jr, T. Li, R. Hardesty, M. Blaylock, Hybrid heating and hot water in multifamily buildings: Demonstration and analysis of integrated boilers and Thermally-Driven heat pumps, ASHRAE Transactions 128 (1) (2022).

[4] J. Winkler, S. Ramaraj, Field validation of air-source heat pumps for cold climates, Tech. Rep. NREL/TP-5500-84745, National Renewable Energy Lab. (NREL), Golden, CO (United States) (May 2023). doi:10.2172/1973090.

[5] T. Clark, D. Aas, C. Li, J. de Villier, M. Levine, J. Landsman, Maryland building decarbonization study, Tech. rep., Energy and Environmental Economics, Inc. (E3) (2021).

[6] NYSERDA, NYS clean heat integrated controls eligibility guidelines, Tech. rep., NYSERDA (2022).

[7] K. Fenaughty, E. Martin, D. Parker, B. Nigusse, An integrated control method for supplemental minisplit heat pumps in existing homes, Tech. Rep. DOE/GO-102021-5492, Univ. of Central Florida, Orlando, FL (United States) (Sep. 2021). doi:10.2172/1814927.

[8] R. Ford, M. Pritoni, A. Sanguinetti, B. Karlin, Categories and functionality of smart home technology for energy management, Building and environment 123 (2017) 543–554. doi:10.1016/j.buildenv.2017.07.020.

[9] J. Drgoňa, J. Arroyo, I. Cupeiro Figueroa, D. Blum, K. Arendt, D. Kim, E. P. Ollé, J. Oravec, M. Wetter, D. L. Vrabie, L. Helsen, All you need to know about model predictive control for buildings, Annual reviews in control 50 (2020) 190–232. doi:10.1016/j.arcontrol.2020.09.001.

[10] K. Zhang, A. Prakash, L. Paul, D. Blum, P. Alstone, J. Zoellick, R. Brown, M. Pritoni, Model predictive control for demand flexibility: Real-world operation of a commercial building with photovoltaic and battery systems, Advances in Applied Energy 7 (100099) (2022) 100099. doi:10.1016/j.adapen.2022.100099.

[11] A. Satchwell, M. Piette, A. Khandekar, J. Granderson, N. Frick, R. Hledik, A. Faruqui, L. Lam, S. Ross, J. Cohen, K. Wang, D. Urigwe, D. Delurey, M. Neukomm, D. Nemtzow, A national roadmap for Grid-Interactive efficient buildings, Tech. rep., Lawrence Berkeley National Lab.(LBNL), Berkeley, CA (United States) (May 2021).

[12] P. Li, D. Vrabie, D. Li, S. C. Bengea, S. Mijanovic, Z. D. O'Neill, Simulation and experimental demonstration of model predictive control in a building HVAC system, Science and Technology for the Built Environment 21 (6) (2015) 721–732. `doi:10.1080/23744731.2015.1061888`.

[13] R. De Coninck, L. Helsen, Practical implementation and evaluation of model predictive control for an office building in brussels, Energy and Buildings 111 (2016) 290–298. `doi:10.1016/j.enbuild.2015.11.014`.

[14] D. Blum, Z. Wang, C. Weyandt, D. Kim, M. Wetter, T. Hong, M. A. Piette, Field demonstration and implementation analysis of model predictive control in an office HVAC system, Applied energy 318 (2022) 119104. `doi:10.1016/j.apenergy.2022.119104`.

[15] D. Kim, J. E. Braun, J. Cai, J. Hu, Development of a plug-and-play multiple RTU coordination control algorithm for small/medium commercial buildings, in: 2015 American Control Conference (ACC), IEEE, Chicago, IL, USA, 2015, pp. 1659–1664. `doi:10.1109/ACC.2015.7170971`.

[16] D. Kim, J. E. Braun, Development, implementation and performance of a model predictive controller for packaged air conditioners in small and medium-sized commercial building applications, Energy and Buildings 178 (2018) 49–60. `doi:10.1016/j.enbuild.2018.08.019`.

[17] D. Kim, J. E. Braun, MPC solution for optimal load shifting for buildings with ON/OFF staged packaged units: Experimental demonstration, and lessons learned, Energy and Buildings 266 (2022) 112118. `doi:10.1016/j.enbuild.2022.112118`.

[18] N. Cotrufo, E. Saloux, J. M. Hardy, J. A. Candanedo, R. Platon, A practical artificial intelligence-based approach for predictive control in commercial and institutional buildings, Energy and Buildings 206 (2020) 109563. `doi:10.1016/j.enbuild.2019.109563`.

[19] G. Demirezen, A. S. Fung, Feasibility of cloud based smart dual fuel switching system (SDFSS) of hybrid residential space heating systems for simultaneous reduction of energy cost and greenhouse gas emission, Energy and Buildings 250 (2021) 111237. `doi:10.1016/j.enbuild.2021.111237`.

[20] Y. Yoon, Y. Li, P. Im, J. Lyons, Potential heating energy and cost savings of dual fuel heat pump controls as a residential building equipment retrofit in the U.S, in: ASHRAE/IBPSA-USA Building Simulation Conference, Vol. 10, ASHRAE and IBPSA-USA, 2022, pp. 243–250. `doi:10.26868/25746308.2022.c029`.

[21] Z. Li, K. Gluesenkamp, B. Shen, J. Munk, H. Zandi, P. Cheekatamarla, , S. Kowalski, Hybrid heat pump controls: Conventional dual fuel versus seamlessly fuel flexible heat pump, in: International Refrigeration and Air Conditioning Conference, 2022, p. Paper 2470.

[22] Air-Conditioning, Heating, and Refrigeration Institute (AHRI), Performance rating of unitary Air-Conditioning and Air-Source heat pump equipment, Tech. Rep. AHRI 210/240-2023 (2020).

[23] National Oceanic and Atmospheric Administration (NOAA), XML feeds of current weather conditions, `https://w1.weather.gov/xml/current_obs/`, accessed: 2022-12-21 (2022).

[24] W. F. Holmgren, C. W. Hansen, M. A. Mikofski, Pvlib python: A python package for modeling solar energy systems, Journal of open source software 3 (29) (2018) 884. `doi:10.21105/joss.00884`.

[25] National Oceanic and Atmospheric Administration (NOAA), Hourly tabular forecast, `https://www.weather.gov/wrh/wxtable`, accessed: 2022-12-20 (2022).

[26] S. Katipamula, J. Haack, G. Hernandez, B. Akyol, J. Hagerman, VOLTTRON: An Open-Source software platform of the future, IEEE Electrification Magazine 4 (4) (2016) 15–22. `doi:10.1109/MELE.2016.2614178`.

[27] L. Paul, F. D. A. Pereira, S. Ham, M. Pritoni, R. Brown, J. Feng, Open building operating system: an Open-Source grid responsive control platform for buildings, in: 2023 ASHRAE Annual Conference at Tampa, FL, 2023.

[28] D. Kim, J. Cai, K. B. Ariyur, J. E. Braun, System identification for building thermal systems under the presence of unmeasured disturbances in closed loop operation: Lumped disturbance modeling approach, Building and environment 107 (2016) 169–180. `doi:10.1016/j.buildenv.2016.07.007`.

[29] D. Kim, J. Cai, J. E. Braun, K. B. Ariyur, System identification for building thermal systems under the presence of unmeasured disturbances in closed loop operation: Theoretical analysis and application, Energy and Buildings 167 (2018) 359–369. `doi:10.1016/j.enbuild.2017.12.007`.

[30] L. Ljung, System identification, in: A. Procházka, J. Uhlíř, P. W. J. Rayner, N. G. Kingsbury (Eds.), Signal Analysis and Prediction, Birkhäuser Boston, Boston, MA, 1998, pp. 163–173. `doi:10.1007/978-1-4612-1768-8\_11`.

[31] J. Braun, N. Chaturvedi, An inverse Gray-Box model for transient building load prediction, HVAC&R Research 8 (1) (2002) 73–99. `doi:10.1080/10789669.2002.10391290`.

[32] H. Madsen, J. M. Schultz, Short time determination of the heat dynamics of buildings, Technical University of Denmark, Department of Civil Engineering, 1993.

[33] P. Virtanen, R. Gommers, T. E. Oliphant, M. Haberland, T. Reddy, D. Cournapeau, E. Burovski, P. Peterson, W. Weckesser, J. Bright, S. J. van der Walt, M. Brett, J. Wilson, K. J. Millman, N. Mayorov, A. R. J. Nelson, E. Jones, R. Kern, E. Larson, C. J. Carey, İ. Polat, Y. Feng, E. W. Moore, J. VanderPlas, D. Laxalde, J. Perktold, R. Cimrman, I. Henriksen, E. A. Quintero, C. R. Harris, A. M. Archibald, A. H. Ribeiro, F. Pedregosa, P. van Mulbregt, SciPy 1.0 Contributors, SciPy 1.0: fundamental algorithms for scientific computing in python, Nature methods 17 (3) (2020) 261–272. `doi:10.1038/s41592-019-0686-2`.

[34] S. Rouchier, M. J. Jiménez, S. Castaño, Sequential monte carlo for on-line parameter estimation of a lumped building energy model, Energy and Buildings 187 (2019) 86–94. `doi:10.1016/j.enbuild.2019.01.045`.

[35] Wikipedia contributors, Latin hypercube sampling, `https://en.wikipedia.org/wiki/Latin_hypercube_sampling`, accessed: 2023-7-16 (2023).

[36] Wikipedia contributors, R-value (insulation), `https://en.wikipedia.org/w/index.php?title=R-value_(insulation)&oldid=1180927466`, accessed: NA-NA-NA (Oct. 2023).

[37] Wikipedia contributors, Table of specific heat capacities, `https://en.wikipedia.org/w/index.php?title=Table_of_specific_heat_capacities&oldid=1178549005`, accessed: NA-NA-NA (Oct. 2023).

[38] D. Simon, Optimal State Estimation: Kalman, H Infinity, and Nonlinear Approaches, John Wiley & Sons, 2006.

[39] S. W. Ham, D. Kim, Hybrid modeling approach for better identification of building thermal network model and improved prediction, 2022, p. Paper 420.

[40] G. Pannocchia, J. B. Rawlings, Disturbance models for offset-free model-predictive control, AIChE journal. American Institute of Chemical Engineers 49 (2) (2003) 426–437. `doi:10.1002/aic.690490213`.

[41] U.S. Department of Energy, Residential Cold-Climate heat pump technology challenge, Tech. Rep. DOE/EE-2523, U.S. Department of Energy (2022).

[42] B. Boyle, pyglpk: Updated fork of t. finley's PyGLPK module, `https://github.com/bradfordboyle/pyglpk`, accessed: 2022-12-15 (2014).

[43] John Kelly Kissock, J. S. Haberl, D. E. Claridge, Inverse modeling toolkit: Numerical algorithms, ASHRAE Transactions 109 (2003) 425–434.

[44] S. Sheather, A Modern Approach to Regression with R, Springer Science & Business Media, 2009.

[45] U.S. Environmental Protection Agency (EPA), Greenhouse gases equivalencies calculator—calculations and references, `https://www.epa.gov/energy/greenhouse-gases-equivalencies-calculator-calculations-and-references`, accessed: 2023-5-24 (2023).

[46] Wikipedia, Climate of New York City — Wikipedia, the free encyclopedia, `http://en.wikipedia.org/w/index.php?title=Climate%20of%20New%20York%20City&oldid=1202907117` (2024).

[47] U.S. Energy Information Administration (EIA), Commercial buildings energy consumption survey (CBECS) data, Tech. rep., U.S. Department of Energy, Washington, DC (2018).